applied sciences

MDPI

Review

Dual-Energy CT Applications in Urological Diseases

Michaela Cellina [1,*], Maria Vittoria Bausano [2], Daniele Pais [2], Vittoria Chiarpenello [2], Marco Costa [2], Zakaria Vincenzo [2], Maurizio Cè [2], Carlo Martinenghi [3], Giancarlo Oliva [1] and Gianpaolo Carrafiello [2,4]

1 Radiology Department, Fatebenefratelli Hospital, ASST Fatebenefratelli Sacco, Piazza Principessa Clotilde 3, 20121 Milan, Italy; linforisonanza@gmail.com
2 Postgraduation School in Radiodiagnostics, Università degli Studi di Milano, Via Festa del Perdono 7, 20122 Milan, Italy; vittoria.chiarpenello@unimi.it (V.C.); maurizioce.md1@gmail.com (M.C.)
3 Radiology Department, San Raffaele Hospital, Via Olgettina 60, 20132 Milan, Italy
4 Radiology Department, Policlinico di Milano Ospedale Maggiore, Fondazione IRCCS Ca' Granda, Via Francesco Sforza 35, 20122 Milan, Italy
* Correspondence: michaela.cellina@asst-fbf-sacco.it

Featured Application: Dual-energy computed tomography has become increasingly applied in clinical practice. Possible applications when studying urological diseases include urinary stone composition analysis, improved detection, and characterization of renal and urothelial lesions. In this narrative review, we aim to provide an overview of the basic principles of dual-energy computed tomography, benefits of its clinical use, and applications in urinary diseases to help radiologists become familiar with this technology.

Abstract: Dual-energy computed tomography (DECT) is a medical imaging technique that uses two different energy levels of X-rays to provide more detailed information about the composition of tissues and materials within the body. DECT technology is still relatively new but different applications have been developed for the urological field. For example, it can be used to analyze the composition of stones to determine whether they are likely to be made up of calcium oxalate, uric acid, or other minerals. This information can help guide treatment decisions, as different types of stones may require different approaches to treatment. The availability of iodine maps helps the differentiation between benign and malignant tumors of the urinary tract, including the bladder, kidneys, and ureters. The iodine maps generated by DECT can provide information on tumor vascularity, which can help in staging and determining the aggressiveness of the tumor. DECT can assess blood flow in the kidneys and detect vascular disorders such as renal artery stenosis or aneurysms. This can be critical for early detection and management of these disorders, which can reduce the risk of renal failure and improve outcomes. DECT is a valuable tool in the urological field that can provide clinicians with detailed and accurate information for the diagnosis and treatment planning of various urological conditions. In this narrative review, we propose an overview of the possible application of DECT in the field of urological diseases.

Keywords: dual-energy computed tomography; urothelial tumors; urologic imaging; renal lesions characterization; iodine maps; urinary stones

Citation: Cellina, M.; Bausano, M.V.; Pais, D.; Chiarpenello, V.; Costa, M.; Vincenzo, Z.; Cè, M.; Martinenghi, C.; Oliva, G.; Carrafiello, G. Dual-Energy CT Applications in Urological Diseases. *Appl. Sci.* **2023**, *13*, 7653. https://doi.org/10.3390/app13137653

Academic Editors: Jan Egger and Biagio Barone

Received: 17 May 2023
Revised: 15 June 2023
Accepted: 27 June 2023
Published: 28 June 2023

1. Introduction

Computed tomography (CT) is a non-invasive diagnostic imaging technique that uses X-rays to obtain detailed images of internal structures in the body.

By accurately detecting and characterizing the wide variety of genitourinary disorders, such as renal stones or aberrant renal parenchyma and renal lesions, CT scanning can guide clinicians to the most suitable treatment [1]. However, there are some drawbacks to the use of traditional CT imaging techniques to assess urological disorders [2].

Dual-energy CT (DECT) is a relatively new technology that improves the visualization and characterization of tissues by utilizing two different energy levels of X-rays [3]. DECT has emerged as a promising tool for the evaluation of urinary tract diseases, providing accurate information about the morphology, function, and composition of the urinary system and able to overcome some of the limitations of traditional CT in this field [4].

In this article, we discuss the principles and advantages of DECT in the study of urinary tract disorders and its potential applications in clinical practice.

2. DECT Principles

In CT scanners, X-rays are generated in the X-ray tube by focusing an electron stream emitted from the cathode into a narrow beam that bombards a small focal spot on the tungsten target anode. These beams are made up of photons with a wide continuum of energies, referred to as "polychromatic X-rays", which create the X-ray spectrum. The maximum photon energy in the X-ray spectrum matches the X-ray tube kilovoltage, meaning that the maximum energy of a 120 kV tube voltage is 120 keV. The X-ray spectrum varies depending on the tube voltage, and the effective X-ray energy is often used as a representative value of a polychromatic X-ray photon spectrum [5]. The effective energy is the energy of a polychromatic X-ray expressed as the energy of a monochromatic X-ray with equivalent interactions, which can be measured using an absorber composed of aluminum or copper [6].

In DECT, virtual monochromatic images (VMIs) obtained at 65–70 keV have the same CT attenuation number (HU) as single-energy CT images obtained at 120 kVp [7]. Therefore, VMIs acquired at 65–70 keV can provide almost equivalent information to single-energy CT images acquired at 120 kVp.

The fundamental principle of DECT is to achieve a good contrast resolution between different materials by exploiting their different spectral properties, that is, differences in the attenuation of X-rays at different photon energies.

At different energy levels, a material has a varying CT number (in Hounsfield units, HU), and the degree of this difference relies on the elemental composition. The CT number of a material is related to its linear attenuation coefficient and is not unique for each material, as similar CT numbers can characterize even materials with different compositions. For this reason, due to their substantial overlap in CT density values, it might be challenging to discern between different materials on single-energy CT scans which therefore provide limited information on tissue composition [8]. DECT images can allow the differentiation and quantification of materials with different elemental compositions by comparing their CT numbers at two different energy levels, and this capability makes DECT a useful tool in the characterization of various materials in a tissue sample.

Different dual-energy technologies are available. Dual-energy CT scanning typically involves two different X-ray energies, usually in the range of 70–100 kVp and 135–150 kVp. Some scanners use two independent X-rays through the fast tube-voltage switching, sequential scan, and dual-source CT systems [9]. Other vendors, however, use only one X-ray source and separate the beam into low- and high-energy spectra either at the detector level (dual-layer system) [10] or at the tube output (split filter system).

Dual-energy analysis methods can be categorized into image data-based analysis and raw data-based analysis. The image-based analysis involves post-processing of the dual-energy scans either before or after the reconstruction of high- and low-energy images to create various dual-energy CT applications [11]. The spatial matching of the reconstructed images is more important than perfectly matching the X-ray paths for high- and low-tube voltages in image-based analysis. Dual-energy data are processed after image reconstruction to create blended images, which are weighted average images at various tube voltages. Other applications include creating iodine map images through material decomposition and virtual non-contrast images by subtracting iodine map images from weighted average images.

The raw data-based analysis involves matching the X-ray paths for high- and low-tube voltages exactly. Material raw data, such as iodine and water, or bone and water, are processed directly through material decomposition, and image reconstruction is then performed. This approach assumes that the human body contains a mixture of two different materials, typically iodine and water, and calculates the content of each material from the original raw dataset. The raw data-based analysis allows for a greater variety of dual-energy CT applications compared to image-based analysis. VMI, electron density, and effective atomic-number analyses require raw data analysis. The choice between raw data- and image-based analyses depends on the dual-energy CT hardware, with raw data-based analysis commonly used with fast tube-voltage switching, sequential scanning, and dual-layer detector systems, while image-based analysis is used with dual-source CT scanners.

3. DECT Benefits

Dual-energy CT is associated with different potential benefits that can be applied in clinical practice.

3.1. Virtual Monochromatic Images

VMIs are CT images that simulate images obtained with monochromatic X-rays of arbitrary energy levels. VMIs at around 65–70 keV are commonly selected as standard images, as they have CT attenuation numbers equivalent to those obtained from single-energy CT scans acquired at 120 kVp [12]. VMIs in this energy range also tend to have lower image noise [13]. Like single-energy CT scans performed at low-tube voltage, VMIs obtained at lower energy levels (e.g., below 60 keV) show increased iodine contrast, which improves the visualization of contrast-enhanced lesions (Figure 1). This characteristic allows for a reduction in the contrast medium dose of 40–60% when using VMIs at 40–50 keV generated from dual-energy CT scans, which can be particularly beneficial in patients with renal insufficiency [14].

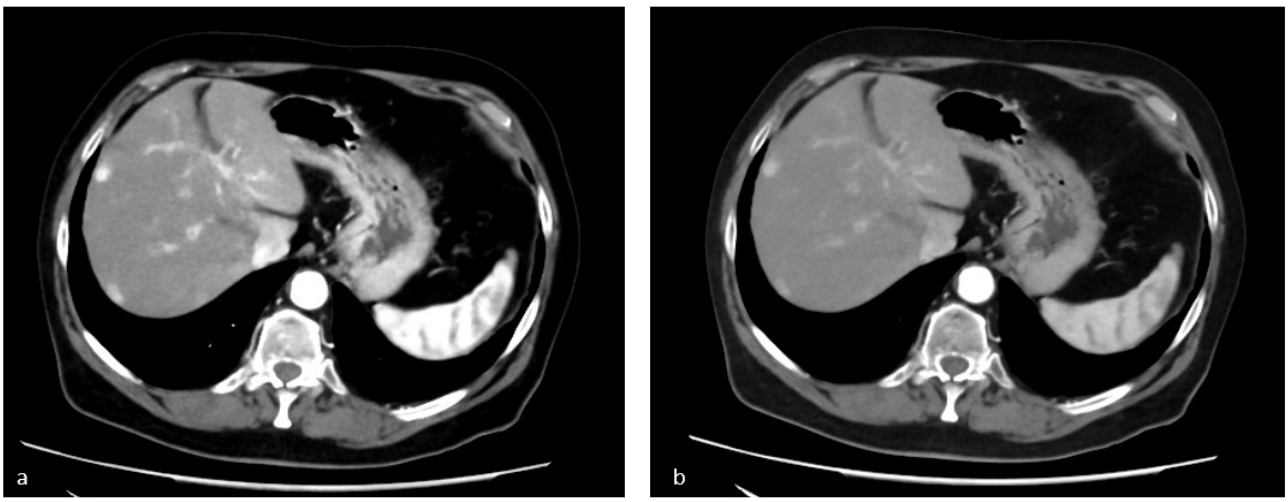

Figure 1. Images of a patient affected by renal clear cell carcinoma. (**a**) Synthetic monochromatic reconstruction at 50 keV; (**b**) reconstruction at 75 keV. Note that hypervascular hepatic lesions are more easily identifiable on (**a**).

Moreover, as a lower energy level results in higher X-ray absorption of iodine from energies close to its k-edge (33.2 keV), the reconstruction of monochromatic images at low keV enhances the conspicuity of hypervascular lesions, such as primitive renal-cell carcinomas and their secondary localizations [4,15–17].

3.2. Virtual Non-Contrast Enhanced Image

Attenuation measurements obtained at the second energy level allow the decomposition of a mixture of two or three materials into its constituent materials and represent the base of virtual non-contrast enhanced (VNC) and iodine images.

VNC images can be generated by subtracting the iodine from the contrast-enhanced DECT images, using three-material decomposition [18]. VNC images facilitate the differentiation of calcifications or high-attenuation materials from iodine-enhanced tissues. The reconstruction of VNC images instead of the acquisition of real unenhanced images allows radiation exposure reduction when unenhanced CT scans are needed (Figure 2) [19].

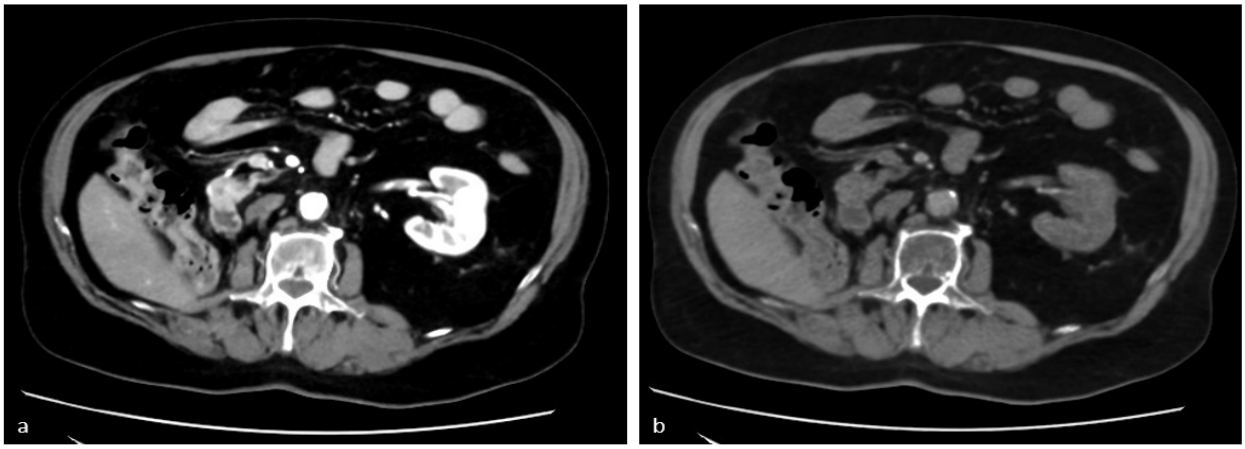

Figure 2. (**a**) Corticomedullary phase acquired in dual energy and corresponding virtual unenhanced image; (**b**) synthetic subtraction of the iodine.

3.3. Iodine Maps

Iodine is used as a contrast agent in CT scans to enhance the visibility of blood vessels, tumors, and other lesions. The iodine map provides information about the distribution and concentration of iodine in tissues (Figure 3) and helps assess the presence and extent of iodine uptake in tissues, providing valuable information for the characterization of lesions, evaluation of tumor vascularity, and monitoring of treatment response [20]. The iodine map images are typically displayed in color, with higher iodine concentrations appearing as brighter colors, allowing for easy visual identification of iodine-rich areas.

Iodine maps can also enhance the visualization of extraluminal iodine components, therefore helping the detection of urinary leakage in trauma patients [21] or as a result of iatrogenic damage [22].

3.4. Spectral HU Curves

VMIs can be utilized to create spectral HU curves: a region of interest (ROI) is drawn in tissue and the average CT number in the ROI at each monochromatic energy level of the VMI, typically ranging from 40 to 140 keV, is obtained automatically. Spectral HU curves provide information about the mean attenuation characteristics of the tissue within the ROI, allowing for the characterization of specific tissue types and aiding in the differential diagnosis. The attenuation of soft tissue and high atomic number materials such as iodine and bone tend to increase at lower energy levels. Water has zero attenuation at all energy levels, while fat shows decreased attenuation at lower energies (Figure 4). The presence of fat can be suggested by observing a curve pattern in the ROI of a specific tissue that indicates decreased attenuation at lower keV. This observation can help diagnose fat-containing diseases, such as lipid-rich plaques, adrenal adenomas, and angiomyolipomas (AML). Spectral HU curves can therefore provide valuable information in identifying tissue characteristics, aiding accurate diagnoses in clinical practice.

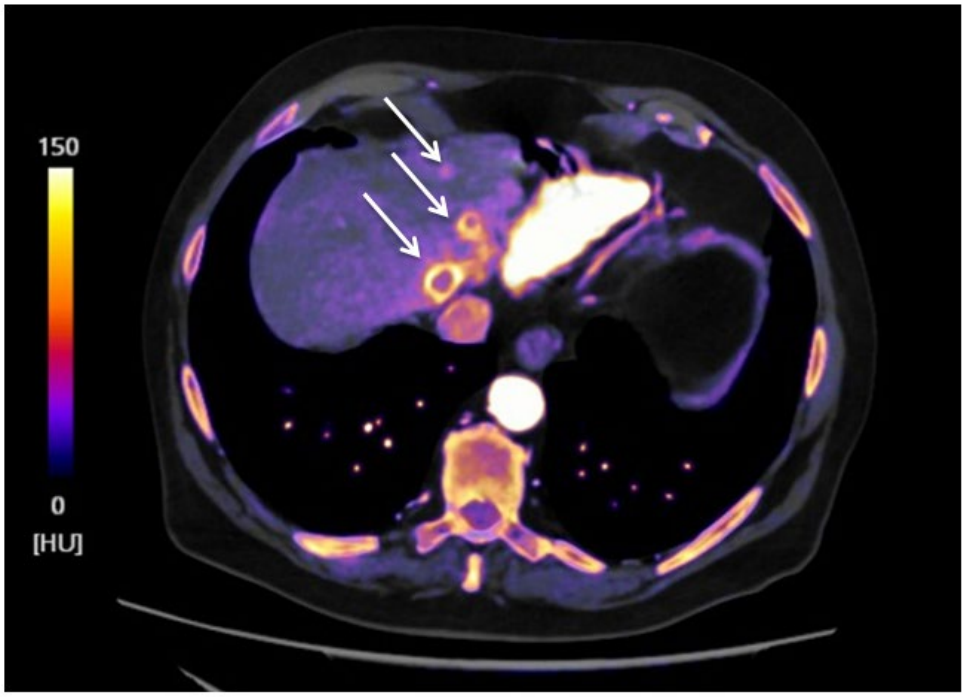

Figure 3. Color-coded overlay-iodine map. Hypervascular hepatic metastases with a peripheral contrast enhancement from a clear cell renal carcinoma. The iodine map highlights the iodine as bright yellow (white arrows). Yellow represents high density of iodine. HU = Hounsfield Units.

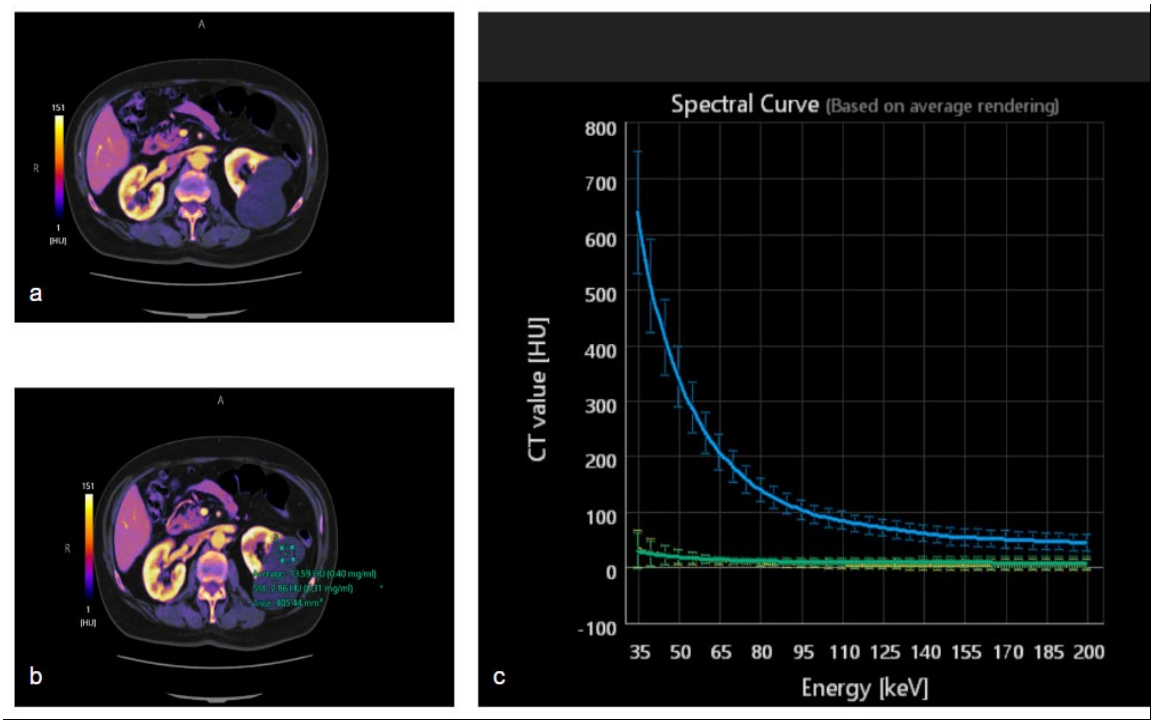

Figure 4. (**a**) Color-coded overlay-iodine map showing two large left renal cysts, visible as devoid of iodine signal. In (**b**), a region of interest in drawn within the cyst to calculate the spectral attenuation curve, and automatically provide the area of the region of interest, the value of HU (Hounsfield Units). In (**c**), the attenuation curve of the cyst in green remains constant, in comparison with the blue one, representing the aortic attenuation curve. The green curve, representing the attenuation behavior of the renal cyst, remains flat, whereas the blue curve of the aorta markedly rises for lower keV to higher Hounsfield unit value.

4. DECT Clinical Applications

In the following subsections, we provide an overview of the possible applications of DECT in the study of urological disorders.

4.1. Characterization of Urinary Stones

CT imaging is the gold standard for detecting nephrolithiasis, as nonenhanced scans have a sensitivity and specificity of >95% [23,24].

The use of CT in the acute presentation of stones is increasing, and it is often the preferred imaging since it can help detect other pathologies responsible for acute abdominal pain.

Uric-acid stones are made up of lower atomic number elements such as carbon, hydrogen, nitrogen, and oxygen, whereas non-uric-acid stones are made up of higher atomic number elements such as calcium, sulfur, and phosphorus [25].

CT imaging may provide insight into the composition of stones by measuring the attenuation in HU, as in general, uric-acid stones have HU between 200 and 400, while calcium oxalate stones have HU between 600 and 1200 [26,27]. However, the ability to characterize stone composition with conventional CT scanning technology is limited, as there is a considerable overlap between the HU of different stone types. Because the diagnosis of uric-acid stones leads to medical dissolution therapy rather than surgical intervention, the characterization of stone composition is useful in clinical decision-making [28].

DECT can allow the differentiation of stone chemical composition by measuring the ratio of calculi attenuation at higher and lower energy.

With dual-source DECT, the characterization is obtained by calculating the calculus ratio of HU at 80 kVp to HU at 140 kVp and plotting it against the attenuation profile of stones with known composition; the most common method employs a three-material decomposition algorithm that assumes every voxel contains a portion of either water, calcium, or uric acid. The quantity of each of these components is then taken into account when assigning a color to the voxels. This tool processes data quickly, taking only a few minutes, and displays acid uric stones with a red overlay and non-acid uric stones with a blue overlay [29].

With fast kilovoltage switching equipment, a plot of effective atomic number versus the attenuation on a VNC image allows the distinction of four categories of calculi: utilizing projection data, single-source DECT equipment estimates the atomic number of particular materials to distinguish between stones made mostly of uric acid, calcium oxalate, cystine, or struvite [30].

Specific changes in attenuation in HU between high- and low-energy spectra allow the differentiation between materials containing similar electron densities but differing photon absorption; through the application of post-processing techniques, such as material decomposition algorithms, the relative proportion of different materials within the stone can be analyzed, helping to identify mixed-composition stones or identify small amounts of certain components [31].

A common DECT protocol for nephrolithiasis begins with a low-dose conventional CT scan to identify potential urinary calculi, followed by a DECT acquisition restricted to the location of the stone. The images are then processed by software application on a three-material decomposition algorithm, which analyzes the stone composition based on the differences in attenuation at the two different energy levels. The software then color codes the stone based on the composition, with stones with behavior like calcium oxalate visualized as blue and stones with behavior similar to uric acid represented as red [32] (Figures 5 and 6).

Using the above acquisition protocol, Thomas et al. calculated an effective radiation dose of 3.4–5.3 mSv [33].

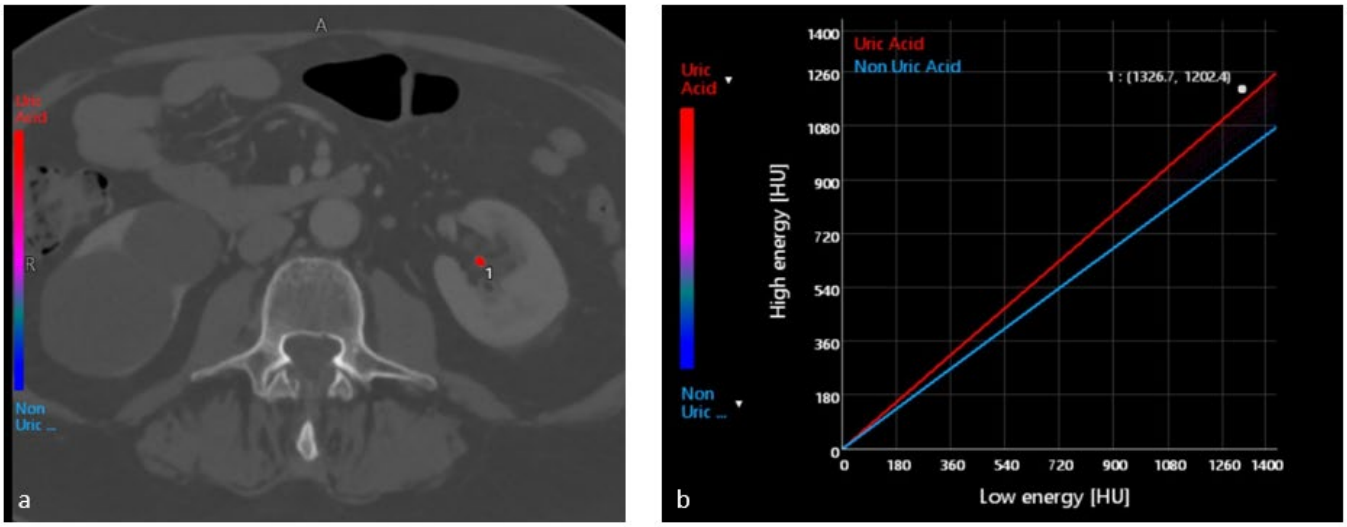

Figure 5. (**a**) Left kidney stone segmented. The composition was revealed to be uric acid (**b**). HU = Hounsfield Units.

Figure 6. Stone composition analysis. (**a**) Intraurethral hyperdense stone; (**b**) automatic segmentation of the stone; (**c**) in the graphic, the stone is placed next to the line of calcium oxide. HU = Hounsfield Units.

When Jepperson et al. compared the radiation exposure of such DECT protocols to that of low-dose and conventional CT scans, they found no significant difference in radiation exposure when compared to the low-dose CT scan alone; moreover, when compared to a conventional CT scan, DECT protocols at 80/140 kVp and 100/140 kVp resulted in a radiation dose reduction of 40% and 31%, respectively [34].

Different studies analyzed the accuracy of DECT in the characterization of urinary stones.

Spek et al. analyzed 213 stones extracted from 64 patients and discovered that UA-containing stones had a different dual-energy index (p = 0.001) compared to pure calcium stones (0.073) and mixed calcium stones (0.077), with a sensitivity of 98.4% and specificity of 98.1% for the differentiation of uric-acid from non-uric-acid stones [35].

Lombardo et al., analyzed DECT images from 33 patients with 62 stones that were spontaneously excreted or treated and found that they had 100% sensitivity and specificity in predicting 15/15 UA stones and 47/47 non-UA stones [36].

Bonatti et al., evaluated nephrolithiasis patients scanned with a low-dose CT followed by a DECT scan: conventional CT correctly detected the composition of 52% (26/50) stones, while DECT correctly detected 90% (45/50) stones; moreover, the conventional CT scan was able to differentiate the uric-acid stones from non-uric-acid stones in 80% (40/50) cases, compared to 96% (48/50) in the DECT scan [37].

In a prospective study, Nestler et al., examined 84 patients who underwent DECT followed by a stone procedure and demonstrated 98.6% consistent results between the DECT and infrared spectrometry. They were able to predict urinary-acid stones from non-urinary-acid stones with a sensitivity of 84.6%, a specificity of 100%, a positive predictive value of 100%, and a negative predictive value of 98.5%. In their model, the combination

of urine pH with DECT resulted in an area under the curve of 0.97 compared to 0.92 for DECT alone, which suggests that combining urine pH with DECT can even enhance the accuracy of DECT [38].

Euler et al., retrospectively included patients who received a low-dose unenhanced DECT for the detection or follow-up of urolithiasis and stone extraction with stone composition analysis. A total of 227 stones in 203 patients were analyzed using X-ray diffraction as the reference standard and identified as 15 uric-acid and 212 non-uric-acid stones with mean size and volume of 4.7 mm × 2.8 mm and 114 mm^3, respectively. Size, volume, CT attenuation, and stone characterization were assessed using DECT post-processing software, and 225 of 227 kidney stones were correctly classified by DECT, with pooled sensitivity, specificity, and accuracy of 1.0 (95% CI: 0.97, 1.00), 0.93 (95% CI: 0.68, 1.00), and 0.99 (95% CI: 0.97, 1.00), respectively. Finally, 82 of 84 stones with a diameter of ≤3 mm were correctly classified [39].

Although still effective, the accuracy of DECT may be slightly diminished in patients with a large body habitus and when the stone size is <3 mm [40,41], this may not be a clinically significant finding, as most stones <3 mm do not warrant intervention and spontaneously pass on their own.

The detection rate of stones is highly dependent of the concentration of iodine in urine; in fact, in a phantom study, >95% of 2–4 mm stones in solution with diluted iodinated contrast medium were identifiable on VNC images, whereas the detection rate was markedly reduced when stones were surrounded by extremely highly concentrated iodine solution. Highly iodinated urine may result in failed iodine subtraction in VNC when the attenuation value of the iodine solution reaches a maximal CT value on low-kV images, thus reducing the sensitivity in stone identification [42].

VNC images created from both nephrographic and pyelographic phases were compared for stone detection [43], with a sensitivity of VNC images from nephrographic phase of 77.5% and from urographic phase of 73.8% (59/80). At high iodine concentration in the excretory system, an incomplete iodine subtraction on VNC images can appear as a rim of brightness along the margins of the collecting system, thus limiting stone identification as the rim could obscure stones or could be misinterpreted as a stone [42].

The sensitivity in stone detection on VNC is dependent on the size of the stones and the iodine concentration in the excretory system [4].

If the acquisition protocol includes a nephrographic and pyelographic phase, the creation of VNC from the nephrographic phase can overcome the problem of iodine density in the collecting system [43].

If a single pyelographic phase with split-bolus technique is acquired, the protocol should be modified to obtain a lower concentration of iodine in the excretory system while maintaining adequate distention through the administration of a lower amount of contrast media and/or a diuretic or patients' hydration [44].

Another limitation is that the stones identified on VNC images often appear smaller than on true unenhanced images [42,43].

Yeo et al., proposed an optimization of the split-bolus technique in patients with suspected urinary stones, by administering 500 mL of water 30 min before the DECT acquisition; first, a 50 mL and an additional 100 mL contrast material after 540 s were administered at 2 mL/s, followed by a 40 mL saline bolus; then, the DECT was acquired 100 s after the contrast medium second bolus, yielding images in combined nephrographic and pyelographic phases; VNC images were then post-processed. This acquisition obtained a sensitivity and diagnostic accuracy of 95.1% and 92.9% for stone detection, respectively [45].

Ureteral stents and percutaneous nephrostomy tubes may occasionally be confounding factors: a study that evaluated 36 different stents from seven manufacturers found that, in general, stents made of polyurethane appeared blue, whereas stents composed of silicon appeared red [46]; therefore, urologists can apply this information to use a stent with the opposite color sequence on DECT when treating a particular stone type.

If the stone is close to the stent, the post-processing software may accidentally incorporate the stent material in calculating the stone composition and incorrectly characterize the stone, with a rate of misdiagnosis reported to be between 4 and 8% [47].

The results of the main studies on stone characterization are listed in Table 1.

Table 1. Main characteristics of studies on renal stone composition analysis with dual-energy computed tomography.

Authors	Number of Patients	Number of Stones	Stone Composition	Gold Standard	Sensitivity	Specificity
Spek et al. [35]	64	213	9 patients with uric acid, 26 patients with calcium oxalate monohydrate, 4 patients with calcium oxalate dihydrate, 7 patients with calcium hydroxyapatite, 1 patient with brushite, 1 patient with cystine, 2 patients with mixed uric acid 14 patients with mixed non-uric acid	Spectroscopy	98.4%	98%
Lombardo et al. [36]	33	62	15 uric acid, 39 calcium oxalate or phosphate, 8 cysteine	Chemical Analysis Urinary Calculi Analysis Kit, DiaSys, Diagnostic System GmbH	100%	100%
Bonatti et al. [37]	30	50	17 uric acid, 29 calcium oxalate or phosphate, 4 cysteine	Infrared spectroscopy	100%	93.9%
Wisenbaugh et al. [48]	Vitro	27	12 uric acid, 6 struvite, 5 cysteine, 4 calcium oxalate	Infrared spectroscopy	92.3%	93%
Nestler et al. [38]	84	144	10 patients uric acid 74 patients non-UA or mixed	Infrared spectroscopy	84.6%	100%
Zhang et al. [49]	67	81	5 uric acid 38 non-UA (31 calcium oxalate 5 uric acid, 2 cysteine) 38 mixed	Fourier-transform infrared spectroscopy	100% (calcium oxalate, cysteine) 77.8% (uric acid)	88.24% (CaOx) 100% (HA-Cys-UA)
Shalini et al. [50]	50		7 uric acid, 43 calcium containing	Infrared spectroscopy		
Shwaky et al. [51]	30	37	8 uric acid, 21 calcium oxalate, 2 calcium phosphates, 4 cysteine, 2 mixed	Crystallography		
Euler et al. [39]	203	227	15 uric acid 175 calcium oxalate, 26 calcium oxalate—apatite, 4 cystine, 3 apatite, 2 calcium oxalate—calcium hydrogen phosphate, 1 triple phosphate, 1 apatite—triple phosphate	X-ray diffraction	100%	93%

4.2. Study of Renal Lesions

Many incidentally discovered renal lesions are incompletely diagnosed by standard CT imaging, creating issues for radiologists and referring physicians.

DECT provides an added value in characterizing renal lesions [52,53], providing higher confidence in lesion characterization, and reducing the need for additional imaging compared to standard single-energy dual-phase computed tomography, while maintaining comparable diagnostic performance to magnetic resonance imaging [54].

DECT has the potential to provide an alternative diagnostic pathway for detecting enhancing renal lesions in patients who may have difficulty adequately breath-holding or cooperating with lengthy MRI examination times, which could result in lower-quality precontrast and postcontrast acquisitions, and it can be also used in patients with pacemakers and other MRI contraindications [55,56].

Even on the contrast-enhanced phase of a standard CT, renal lesions with attenuation close to water can be easily identified as simple cysts; however, a double-phased examination is needed, with one phase before and one after intravenous contrast administration, to determine whether a lesion with attenuation higher than water represents a nonenhancing hyperdense cyst or an enhancing solid renal mass [57]. To determine whether a lesion enhances or not, the measured difference in attenuation between the two phases is used: enhancement is defined as any attenuation increase of 10 HU by some radiologists, while others define true enhancement as an attenuation increase of 20 HU [57].

VNC images generated from enhanced DECT acquisition have been proven to correlate well with true unenhanced images and the attenuation measurements on the VNC are considered reasonably approximate to true unenhanced images [58].

Iodine maps can be obtained from contrast enhanced DECT acquisitions through material decomposition algorithms and allow the reliable identification of enhancing lesions [59]. Using a color-coded overlay display, an iodine map graphically depicts iodine contrast inside the interrogated voxels: as a result, nonenhancing renal cysts and enhancing solid renal tumors can be distinguished on the map reconstructed from single-phase postcontrast datasets, where nonenhancing renal cysts lack iodine content, whereas solid enhancing renal tumors uptake the iodine contrast medium [8,9,19]. Color-coded iodine overlay images allows an easy visual differentiation of enhancing from nonenhancing renal lesions, as enhancing masses contain color-coded pixels within them. Moreover, they can be useful for an easy visual assessment of patients with multiple renal lesions, such as polycystic kidney disease, as enhancing lesions can be easily distinguished by cysts and hemorrhagic cysts [60].

The analysis of iodine map helped the characterization of hyperdense renal masses incidentally discovered on a single-phase enhanced DECT, particularly in lesions sized $\geq$1.5 cm [61].

DECT enables an improved abnormalities characterization through the quantification of the iodine amount in each image pixel. An extra tool accessible with DECT datasets is represented by spectral attenuation curves [62]: when an ROI is drawn within a lesion, the lesion attenuation profile in the multi-energy scale can be assessed. Iodine-containing renal lesions can be distinguished from non-iodine-containing cysts because iodine attenuation increases at lower energies ("upward-curve-type"); in contrast, cyst attenuation levels remain constant across the whole monochromatic multi-energy range ("flat-curve-type") [9] (Figure 7).

In a study by Moleesaide et al., 78 renal incidental lesions (24 enhancing; 54 nonenhancing) measuring 1–4 cm were studied with a rapid kilovoltage-switching DECT and the results were compared with histology: the analysis of the monochromatic images and of the iodine curves significantly differentiated the enhancing and nonenhancing lesions ($p < 0.001$) [63].

Proper preoperative pathological classification of RCC is essential for evaluating the malignancy of the tumor and selecting the appropriate surgical approach. DECT can be used to determine the tumor blood supply of a lesion. In fact, tumor blood supply types are correlated with pathological grade, with well-differentiated clear-cell renal-cell carcinoma (ccRCC) exhibiting mature arteries and enhanced vascular permeability, and poorly differentiated ccRCC exhibiting hemodynamic abnormalities and arteriovenous shunts [64].

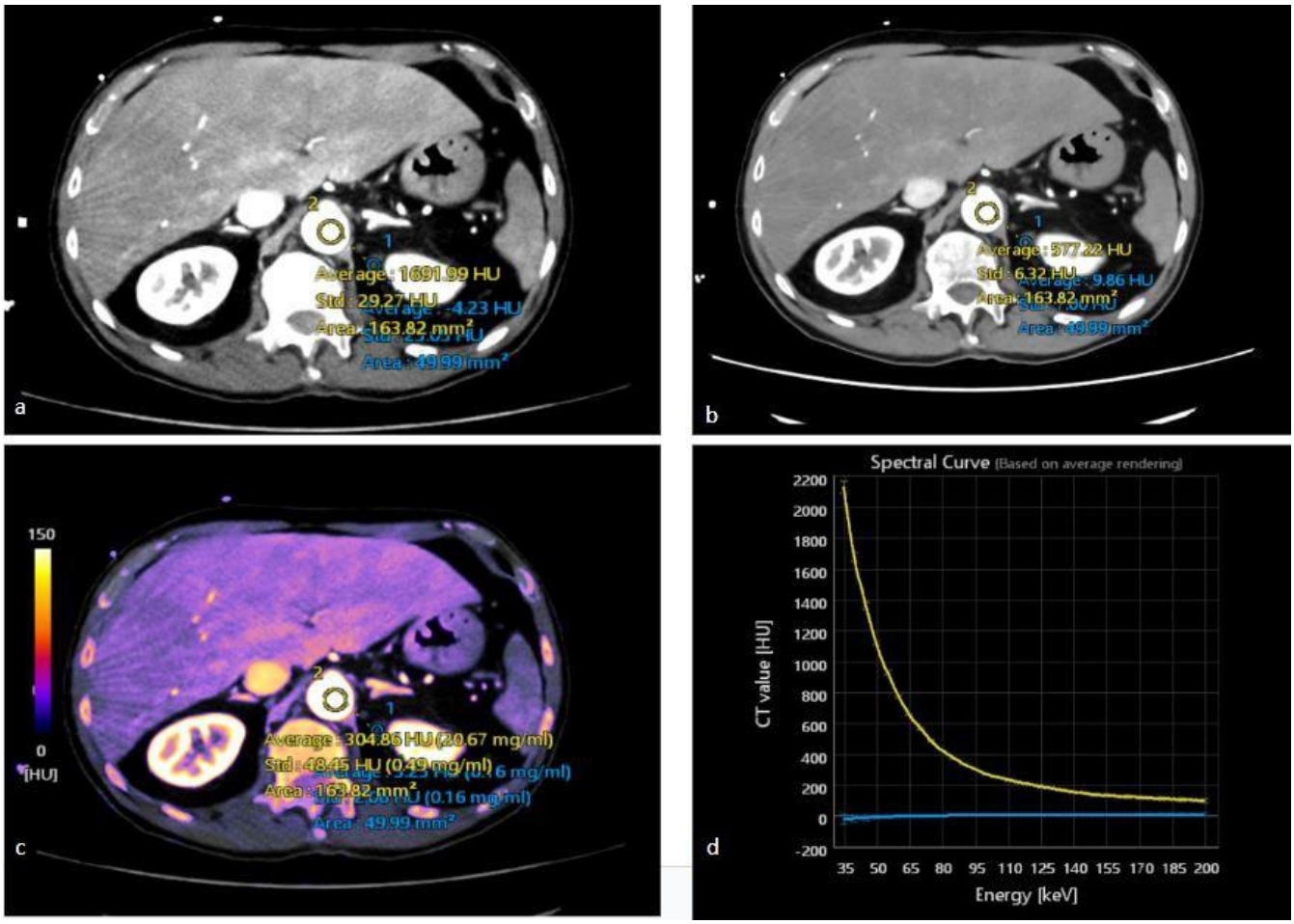

Figure 7. Example of a spectral attenuation curve of a small left renal cyst. (**a**) Monochromatic image at 40 keV; (**b**) monochromatic image at 80 keV; (**c**) iodine map showing no contrast enhancement within the cyst, confirmed by the flat-curve-type of the cyst in blue (**d**), compared with the upward-curve-type of the aorta in yellow that shows a rise in Hounsfield units for low energy levels. HU = Hounsfield Units.

Differentiating between papillary (p) RCC and ccRCC can be challenging in imaging [65], but a recent study by Marcon et al., indicated that ccRCC had a significantly higher iodine concentration than pRCC, and a positive correlation was found between the iodine concentration and microvascular density on DECT, and a cut-off value of $\leq$3.1 mg/mL at iodine concentration analysis allowed the diagnosis of pRCC with an accuracy of 86.8% [56].

DECT can also be used in the characterization of AML. AML is typically characterized by macroscopic fat, which can be confirmed by visual analysis and attenuation measurements of <−10 to −15 Hounsfield units (HU) on CT. However, misclassification of AML can occur in cases of fat-poor AML or when imaging with only contrast-enhanced CT due to elevated attenuation measurements. This can happen in small AMLs due to volume averaging of adjacent renal parenchyma or pseudo enhancement, as well as due to the presence of internal enhancing vessels within the AML (Figure 8). Up to one-third of AML may be indeterminate by HU measurements when evaluating only contrast-enhanced CT, leading to recall for further imaging such as dedicated thin-section unenhanced CT or MRI for confirmation.

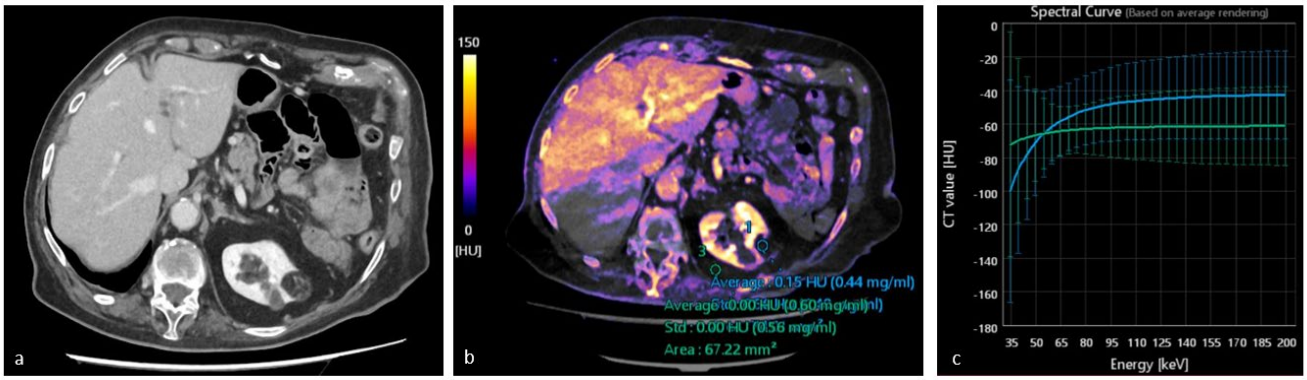

Figure 8. (**a**) Left renal lesion with prevalent fat tissue density, but with inhomogeneous content; (**b**) the color-coded overlay-iodine map demonstrates the absence of intralesional contrast enhancement, confirmed by the iodine analysis (**c**). The lesion was characterized as an angiomyolipoma. The curve of angiomyolipoma (blue) shows a reduction in the attenuation values at lower energies with attenuation values in line with that of the fat tissue (green). HU = Hounsfield Units.

However, since the introduction of DECT, other analysis systems such as iodine maps, VMI with spectral curves, atomic-number maps, and fat maps have been developed to improve the signal fat and increase the sensitivity of CT in the recognition of intralesional adipose tissue.

Material-specific fat images derived from DECT seem to be highly accurate in detecting areas of macroscopic fat, with fat concentration measurements being useful to confirm the presence of macroscopic fat in renal masses and establish the diagnosis of renal AML when non-contrast-enhanced CT is unavailable. In cases where DECT was used, the nodule could have been definitively characterized as containing macroscopic fat without recalling the patient for additional imaging [66].

In a prospective study including 95 patients with renal tumors, the authors analyzed the absolute enhancement, the enhancement ratio, and iodine content of each lesion on nephrographic phase images and were able to distinguish fat-poor AML from renal malignant lesions [67].

In Table 2, we summarize the results of the above studies.

Table 2. Characteristics and results on the studies dealing with renal lesion characterization with DECT.

Author	Investigated Pathology	N° of Patients	Gold Standard	Acquisition Phase in DECT	Main Results
Graser et al. [53]	Ultrasound-based suspicion of a renal mass	202	Histopathology	Nephrographic phase DECT	-96.0% patients with malignancy and 93.2% without malignancy were correctly identified -overall accuracy: 94.6% -The omission of the true unenhanced phase led to a 48.9 ± 7.0% dose reduction.
Pourvaziri et al. [54]	Renal lesions	69	**Simple cysts**: all distinct features of a simple cyst on both CT and MR. **Proteinaceous/hemorrhagic cyst**: the characteristic appearance of it on both CT and MRI. **Enhancing lesions**: histopathology or unequivocal signs of enhancement on both CT and MRI.	Nephrographic phase DECT	-The pooled diagnostic confidence scores for the three readers were comparable for the DECT and MRI scans (pooled DECT mean = 4.78, SD: 0.48 vs. pooled MRI mean = 4.78, SD: 0.51, *p*-value: 0.96). -The inter-reader agreement was almost perfect for DECT and MRI (kappa: 0.8–1) -Comparable diagnostic accuracy between single energy CT, DECT, and MRI (*p*-value > 0.05).

Table 2. *Cont.*

Author	Investigated Pathology	N° of Patients	Gold Standard	Acquisition Phase in DECT	Main Results
McGrath et al. [55]	Renal masses	24	Histopathology	Corticomedullary phase (CMP) and late nephrographic phase (LNP)	-No significant difference in diagnostic accuracy comparing subjective enhancement by MRI and DECT iodine map.
Alanee et al. [68]	Papillary renal-cell carcinoma (pRCC)	1	Histopathology	Not specified	-Iodine maps allow for their accurate characterization as solid masses.
Graser et al. [58]	Renal masses	110	Histopathology, contrast-enhanced US, follow-up CT	Nephrographic phase DECT	-In all but three patients, radiologists accepted virtual non-contrast images as a replacement for true non-contrast images. -Mean dose reduction by omitting the true non-contrast scan was 35.05%.
Cha et al. [61]	Hyperdense renal lesions incidentally detected on single-phase postcontrast CT	79	In patients who underwent surgical resection or biopsy, histopathological reports were used as the reference standard. If histopathology was not confirmed, follow-up imaging was used to make a final diagnosis.	Corticomedullary phase (CMP) and late nephrographic phase (LNP)	-For differentiating between solid and benign cystic lesions, the specificity and accuracy of all lesions and lesions < 1.5 cm were statistically lower in iodine images than in linearly blended images; for lesions $\geq$ 1.5 cm, they were not statistically different. -For all types of lesions $\geq$ 1.5 cm, the CT numbers between linearly blended and iodine images and between true non-contrast and virtual non-contrast images were not statistically different ($p > 0.05$).
Ascenti et al. [62]	Complex cystic renal masses	79	Surgical resections, biopsy, percutaneous drainage, and imaging follow-up for a minimum of 12 months were used to determine the outcome.	Corticomedullary phase DECT	-Virtual non-contrast and true unenhanced evaluation to identify complex cystic renal masses was judged acceptable in 97.2% of cases. -Color-coded iodine-overlay images allowed the exclusion of enhancement with a significantly ($p < 0.03$) higher level of confidence (score 1, $n = 22$; score 2, $n = 3$) than on true unenhanced and blended images.
Moleesaide et al. [63]	Renal lesions	46	Histopathology, interval size-change, US, follow-up CT, MRI T2 sequences	Nephrographic phase DECT	-All datasets yielded a high diagnostic accuracy of 96% for reader 1 and 95% for reader 2. -A ΔHU threshold of 20 HU yielded an accuracy of 100%. -Visual analysis of the curve pattern also yielded high accuracy of 94%.
Wei et al. [64]	Clear cell RCC (ccRCC)	62	Histopathology	Cortex phase (CP) and parenchymal phase (PP)	-In the qualitative analysis of the imaging features observed during the combined CP and PP, sensitivity and specificity of 80% and 77.8%, respectively, were achieved for differentiating between low- and high-grade ccRCC. -The quantitative parameters analysis with CT spectral imaging compared with qualitative CT image analysis improved the sensitivity from 80% to 90.3% and the specificity from 77.8% to 87.5%.
Marcon et al. [56]	Clear-cell RCC and papillary RCC	53 patients with clear-cell RCC (ccRCC) and 15 with papillary RCC (pRCC)	Histopathology	Nephrographic phase DECT	-Analysis of iodine concentration (IC) showed a significant difference between pRCC and ccRCC ($p < 0.001$). -Mean IC for ccRCC was 4.83 $\pm$ 1.75 mg/mL (range 2.2–11.5 mg/mL); for pRCC, it was 2.53 $\pm$ 1.59 (range 0.4–6.6 mg/mL). -ROC analysis revealed an ideal cutoff value of $\leq$3.1 mg/mL (AUC 0.866, $p < 0.001$) regarding the distinction between pRCCs and ccRCCs. -The calculated specificity was 90.6%, with a sensitivity of 73.3% and an accuracy of 86.8%.
Walker et al. [66]	Angiomyolipoma (AML)	25 patients with diagnosed AML and 44 patients with renal masses (control group)	Presence of internal macroscopic fat at true 120 kVp non-contrast-enhanced CT (NECT) with an area of macroscopic fat measuring <−15 HU in density (24/25) or histopathology from 18 G core needle biopsy when macroscopic fat was not present (1/25).	Corticomedullary phase DECT	-At DECT, fat concentration was higher in AML ($p < 0.001$). -AUC to diagnose AML using −206.0 mg/mL threshold was 0.98 (95% CI 0.95–1.0) with sensitivity/specificity of 92.0%/96.7%. -Of AML, 8.0% (2/25)were incorrectly classified; one of these was fat-poor.

4.3. Study of the Bladder and Ureters

Urothelial tumors (UC) are divided into upper-tract urothelial carcinoma (UTUC), involving calico-pyelic cavities and ureters, and lower-tract urothelial carcinoma (LTUC), involving bladder (90–95%) and proximal urethra.

Compared to cystoscopy, which represents the gold standard in bladder cancer diagnosis, URO-CT is not a useful method in the identification of LTUC but is useful in follow-up and in muscle-invasive and metastatic bladder cancer to evaluate its extension [1,69], multiple high-risk tumors, or in the trigone vesica localization. On the other hand, CT urography is the most sensitive method for the identification of UTUC [70].

DECT appears to be better both in the diagnosis and in the follow-up of UC because it has many benefits in the study of them, such as less exposure to ionizing radiation and iodinated contrast agents [71,72].

UC can be visible on CT as small filling defects, mass lesions, vegetations, or wall thickening [71].

The detection of UC relies on the contrast between the tumor and an adjacent non-pathological urothelial wall or surrounding urine.

During the parenchymal phase of contrast enhancement, UC shows increased contrast enhancement, while the urine is unenhanced and the surrounding normal urothelium shows minimal enhancement; in the urographic phase instead, UC reduces the enhancement and becomes hypodense, and iodinated urine shows high density. The higher contrast is, however, shown in the corticomedullary phase, related to their extensive vascularity. In this phase, any focal area of urothelial hyperenhancement should be considered suspicious for malignancy [73,74].

DECT offers the possibility of reducing radiation exposure due to VNC, avoiding baseline scans starting from postcontrast acquisition and removing iodine from soft tissues [7,75].

The combination of VNC images and the split-bolus protocol have been proposed to obtain a further reduction in radiation exposure [70].

The nephrographic and excretory phases are acquired at the same time in the split-bolus protocol, and the contrast medium is administered in two separate injections: the first part (usually one-third or half) is injected; the second part (usually a dose greater than or equal to the first one) is then injected about 5–10 min later, and the combined nephrographic–excretory-phase images are acquired at 2–5 min when the kidneys show enhancement of the renal parenchyma [12]. The ratio between the first and second contrast portions of the split bolus, as well as the ideal delay time, vary widely among different studies [12].

This protocol allows evaluating renal masses and UC correctly thanks to the concurrent visualization of the cortico-medullary, nephrographic, and excretory phases with a single scan [76,77].

The possibility of reducing the amount of contrast material administration is another advantage of DECT, especially in the case of multiple follow-ups or patients with kidney failure or older patients with multiple comorbidities [78]. This is possible because of the use of low-energy images which allow for obtaining higher contrast images, due to the higher attenuation coefficients at lower energy, and increased tumor conspicuity [7]. Low-dose VMI allows a better quantitative rating of primary UC than conventional venous-phase imaging with similar qualitative ratings for both primary UC and metastases [79].

Another issue that DECT can help with is beam-hardening artifacts caused by metal prostheses, which falsify pelvic evaluations [80]. These artifacts can be reduced due to VMI with doses between 105 keV and 150 keV [81–83] at the expense of contrast and, consequently, the worst evaluation of soft tissues, albeit with noise reduction. Reconstruction algorithms that use datasets at different energy levels can help to overcome this obstacle [84,85].

The evaluation of the contrast produced between the tumor and the surrounding normal urothelial wall or overlying urine is the basis for the detection of urothelial tumors (Figures 9 and 10).

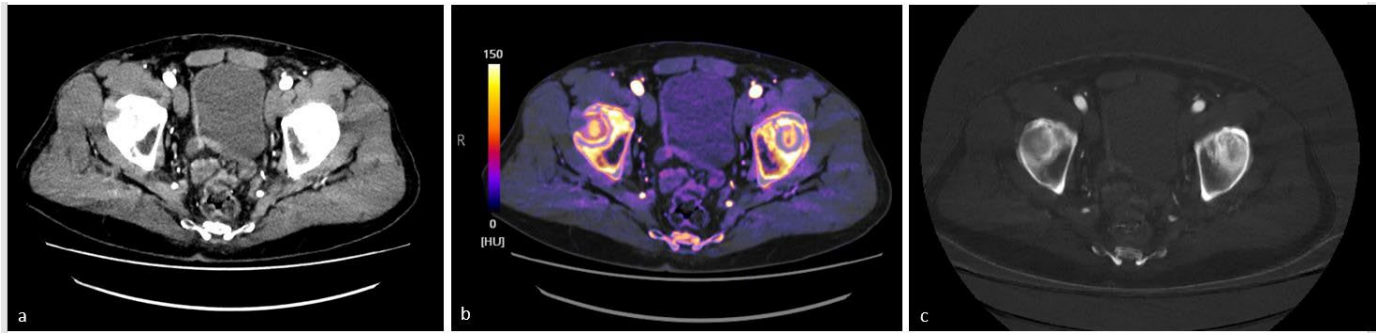

Figure 9. (**a**) Synthetic monoenergetic reconstruction at 40 keV increases the visualization of contrast enhancement of the right bladder wall, papillary urothelium, and distal right ureter in a patient previously treated for bladder cancer. The iodine map (**b**) and the iodine image (**c**) confirm the presence of pathological contrast enhancement. This finding resulted from a local disease relapse.

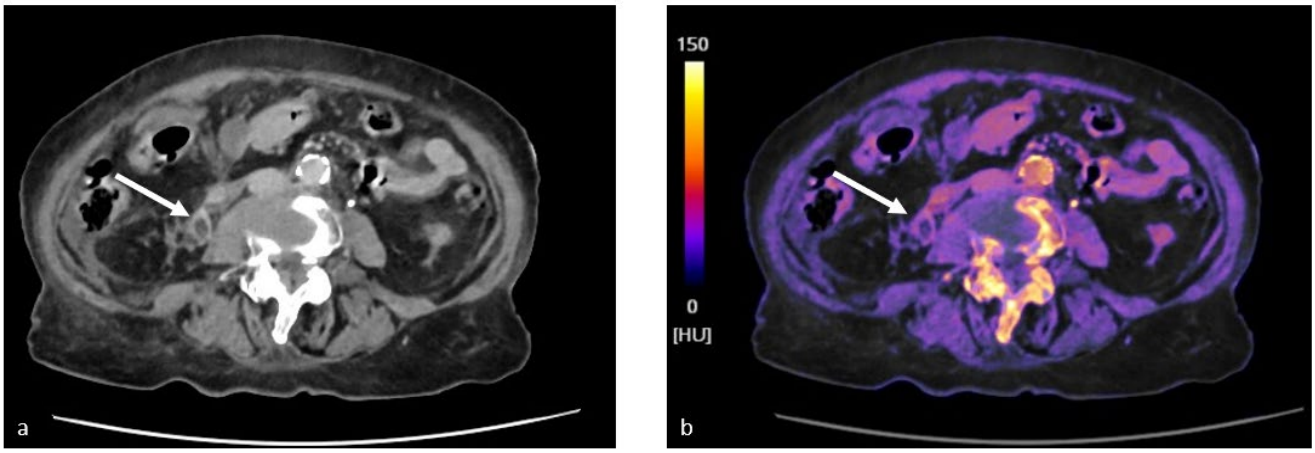

Figure 10. Incidental detection of right ureteral cancer (white arrows). (**a**) Monochromatic image at 40 keV showing a concentric thickening of the ureteral wall, confirmed on the iodine color map (**b**).

When contrast medium is administered, urothelial tumors typically show a moderate enhancement during the nephrographic phase, while the healthy urothelial tissue around them impregnates poorly and the urine is still hypodense. However, the most common diagnostic feature of urothelial tumors is represented by a filling defect on pyelographic phase images, as shown by recent studies.

The CT sensitivity in the detection of these tumors may be improved by the early enhancement as a diagnostic criterion [85]. Nakagawa et al. [86], in fact, analyzed VMI at 40 keV of 52 patients with histological demonstration of bladder cancer in comparison with synthetics 120 kVp reconstructions and demonstrated that, in VMI at 40 keV, the difference in CT number between the cancer and bladder wall was significantly higher and that these images were preferred by the readers with a statistically significant difference.

In another study, the contrast-to-noise ratio of urothelial carcinoma to adjacent bladder wall resulted in significantly higher excretory-phase VMIs at 40 keV when compared to venous-phase CT [79].

Hansen et al. [87] proposed a dedicated protocol for urothelial tumors including a dual-energy 35 s arterial phase and an 8 min nephrographic–excretory phase. The combination of these two acquisitions allowed the detection of urothelial tumors with a sensitivity of 97.3%.

The characteristics of the above studies are listed in Table 3.

Table 3. Characteristics and results of the studies dealing with urothelial and bladder cancer characterization with dual-energy CT.

Authors	Pathologies	N° pz	Acquisition Phase in DECT	Main Results
Chen et al. [77]	Hematuria	171	Late-venous phase	-Sensitivity, specificity, and accuracy were 98.7%, 98.9%, and 98.8%, respectively, for the one-step approach to malignant mass detection and 98.7%, 97.9%, and 98.3% for the dual-phase approach ($p > 0.05$ for all comparisons). -Omitting the unenhanced scan reduced the mean radiation dose from 15.4 to 6.7 mSv.
Zopfs et al. [79]	Urothelial carcinoma	26	Late-venous and excretory phase	-In comparison to venous-phase CT, attenuation, and signal-to-noise-ratio in excretory-phase VMI 40 keV were higher ($p < 0.001$). -Regarding image noise, no significant difference was found between venous-phase CT and excretory-phase VMI 40 keV (*p*-range: 0.08–1.00). -Contrast-to-noise ratio of urothelial carcinoma to circumjacent bladder wall was significantly higher in excretory-phase VMI40 keV compared to venous-phase CT. -Subjective vessel contrast and delineation of primary tumor and distant metastases received equivalent or higher Likert scores in excretory-phase VMI40 keV than in venous phase.
Nakagawa et al. [86]	Bladder cancer	52	Nephrogenic phases	-The mean difference in CT number between the cancer and bladder wall value at 40 keV was significantly higher than that of virtual 120 kVp (80.5 ± 54 vs. 11.4 ± 12.5 HU, $p < 0.01$). -Average scores of subjective evaluations in the virtual-120 kVp and 40 keV images were 1.7 ± 1.2 and 2.1 ± 1.2, respectively ($p < 0.001$).
Hansen et al. [87]	Macroscopic hematuria and known or suspected neoplastic disease	56	Arterial and excretory phase	-Urothelial tumors were identified on 35 s series, 8 min series, and both series combined, with sensitivity of 91.9%, 83.4%, and 97.3%, respectively. -Urothelial tumors showed stronger virtual enhancement ($p = 0.02$) and higher iodine concentration ($p = 0.03$) than lesions of other origin. -Distinction between urothelial tumors and nontumoral lesions was possible with sensitivity of 91.9%.

5. Limitations

DECT is a valuable technique, but it is associated with some limitations.

DECT scanning has some requirements: high- and low-energy data should be acquired simultaneously or with a small interval, as a prolonged time gap (for example, related to patient movement, gastrointestinal peristalsis, or the flow of contrast material) results in a spatial mismatch between the two datasets, affecting the image quality. As dual-energy CT analysis is based on the contrast between the X-ray absorption of the two-energy data, the energy difference between the two-energy data should be large; a smaller energy difference instead results in a lower contrast-to-noise ratio.

Another limitation associated with DECT and CT imaging, in general, is radiation exposure.

Radiation exposure should not exceed 50 mSv per year or 100 mSv during a 5-year period, according to the International Commission on Radiological Protection standards. [88]: although a single CT scan would not exceed these thresholds, nephrolithiasis is frequently a lifelong condition that manifests early in life. The accumulation of scans results in a cumulative radiation exposure. A solution is represented by the application of a tin filter. Second-generation DECT scans were the first equipped with a tin filter in front of both X-ray tubes, which effectively absorbs primarily low-energy photons of limited diagnostic utility, resulting in a reduced radiation exposure to patients [89].

Apfaltrer et al., for example, used a tin filter and a low-dose protocol and reported overall high image quality with a calculated mean overall effective dose of 3.34 ± 1.84 mSv [90].

Nestler et al., also utilized a tin filter and calculated a mean overall effective dose of 3.38 ± 1.93 mSv [38].

A study by Dewes et al., also supported the usage of the tin filter, demonstrating a 23% reduction in radiation exposure, a decrease in background noise, and improved image quality when compared to DECT without a tin filter [91].

Image quality of VNC images can be decreased by a rough texture and poor spatial resolution or shows a smooth appearance not appreciated by radiologists [58,92,93].

Another issue with VNC images is the incomplete iodine removal in cases of very high iodine concentration, and loss of tiny and not highly attenuated calcific areas during the VNC reconstruction process, as well as higher image noise and reduced conspicuity of calcification in renal masses that can affect kidney lesion interpretation [4].

The use of DECT can be contraindicated in obese patients, as larger bodies may result in greater image noise and reduced image quality (related to the limited number of photons reaching the detectors), affecting material decomposition and limiting tissue characterization [94]; moreover, beam hardening artifacts are more evident in obese subjects because of the longer path where the X-ray beam is attenuated [95]. Therefore, patient selection for DECT acquisition should be established after assessing the patients' size on the scout radiograph [96].

Another limitation of DECT is represented by the equipment cost, as a DECT scanner can be a costly acquisition for healthcare systems: whereas 16-slice CT scanners average USD 402,000 and 64- and 80-slice scanners average USD 549,000, a DECT scanner can average USD 1.29 million and possibly even more [97].

6. Conclusions

DECT technology provides significant advances in the study of renal and excretory system disorders.

DECT is effective in the characterization of urinary stones, providing useful information for the patients' management. This technique can improve the characterization of incidental renal masses in clinical practice and decreases radiation exposure and the need for further examinations.

Radiologists and clinicians should be familiar with possible applications and apply them in everyday clinical practice.

Due to the continuous advancements in hardware and software, the use of DECT in urological disease is destined to grow and spread.

Author Contributions: Conceptualization, M.C. (Michaela Cellina), M.C. (Maurizio Cè) and C.M.; methodology, M.C. (Michaela Cellina), G.O., M.C. (Marco Costa) and V.C.; validation, Z.V., M.V.B. and M.C. (Maurizio Cè); formal analysis, D.P., Z.V. and M.C. (Marco Costa); investigation, V.C. and M.C. (Maurizio Cè); writing—original draft preparation, M.C. (Michaela Cellina), D.P., M.V.B., V.C., M.C. (Marco Costa) and Z.V.; writing—review and editing, M.C. (Michaela Cellina), C.M. and G.C.; visualization, G.C.; supervision, G.O., G.C. and C.M.; project administration, G.O., C.M. and G.C. All authors have read and agreed to the published version of the manuscript.

Funding: This research received no external funding.

Institutional Review Board Statement: Not applicable.

Informed Consent Statement: Not applicable.

Data Availability Statement: Not applicable.

Conflicts of Interest: The authors declare no conflict of interest.

References

1. Ascenti, G.; Cicero, G.; Bertelli, E.; Papa, M.; Gentili, F.; Ciccone, V.; Manetta, R.; Gandolfo, N.; Cardone, G.; Miele, V. CT-Urography: A Nationwide Survey by the Italian Board of Urogenital Radiology. *Radiol. Med.* **2022**, *127*, 577–588. [CrossRef]
2. Joffe, S.A.; Servaes, S.; Okon, S.; Horowitz, M. Multi-Detector Row CT Urography in the Evaluation of Hematuria. *Radiogr. Rev. Publ. Radiol. Soc. N. Am. Inc.* **2003**, *23*, 1441–1455, Discussion in 1455–1456. [CrossRef]
3. Cicero, G.; Mazziotti, S.; Silipigni, S.; Blandino, A.; Cantisani, V.; Pergolizzi, S.; D'Angelo, T.; Stagno, A.; Maimone, S.; Squadrito, G.; et al. Dual-Energy CT Quantification of Fractional Extracellular Space in Cirrhotic Patients: Comparison between Early and Delayed Equilibrium Phases and Correlation with Oesophageal Varices. *Radiol. Med.* **2021**, *126*, 761–767. [CrossRef]
4. Kaza, R.K.; Platt, J.F.; Megibow, A.J. Dual-Energy CT of the Urinary Tract. *Abdom. Imaging* **2013**, *38*, 167–179. [CrossRef]
5. Tatsugami, F.; Higaki, T.; Nakamura, Y.; Honda, Y.; Awai, K. Dual-Energy CT: Minimal Essentials for Radiologists. *Jpn. J. Radiol.* **2022**, *40*, 547–559. [CrossRef]

6. Matsumoto, K.; Jinzaki, M.; Tanami, Y.; Ueno, A.; Yamada, M.; Kuribayashi, S. Virtual Monochromatic Spectral Imaging with Fast Kilovoltage Switching: Improved Image Quality as Compared with That Obtained with Conventional 120-KVp CT. *Radiology* **2011**, *259*, 257–262. [CrossRef]
7. Yang, L.; Sun, J.; Li, J.; Peng, Y. Dual-Energy Spectral CT Imaging of Pulmonary Embolism with Mycoplasma Pneumoniae Pneumonia in Children. *Radiol. Med.* **2022**, *127*, 154–161. [CrossRef]
8. McCollough, C.H.; Leng, S.; Yu, L.; Fletcher, J.G. Dual- and Multi-Energy CT: Principles, Technical Approaches, and Clinical Applications. *Radiology* **2015**, *276*, 637–653. [CrossRef]
9. Mileto, A.; Sofue, K.; Marin, D. Imaging the Renal Lesion with Dual-Energy Multidetector CT and Multi-Energy Applications in Clinical Practice: What Can It Truly Do for You? *Eur. Radiol.* **2016**, *26*, 3677–3690. [CrossRef]
10. Ergun, D.L.; Mistretta, C.A.; Brown, D.E.; Bystrianyk, R.T.; Sze, W.K.; Kelcz, F.; Naidich, D.P. Single-Exposure Dual-Energy Computed Radiography: Improved Detection and Processing. *Radiology* **1990**, *174*, 243–249. [CrossRef]
11. Fernández-Pérez, G.C.; Fraga Piñeiro, C.; Oñate Miranda, M.; Díez Blanco, M.; Mato Chaín, J.; Collazos Martínez, M.A. Dual-Energy CT: Technical Considerations and Clinical Applications. *Radiol. Engl. Ed.* **2022**, *64*, 445–455. [CrossRef]
12. Cellina, M.; Cè, M.; Rossini, N.; Cacioppa, L.M.; Ascenti, V.; Carrafiello, G.; Floridi, C. Computed Tomography Urography: State of the Art and Beyond. *Tomography* **2023**, *9*, 909–930. [CrossRef]
13. Pomerantz, S.R.; Kamalian, S.; Zhang, D.; Gupta, R.; Rapalino, O.; Sahani, D.V.; Lev, M.H. Virtual Monochromatic Reconstruction of Dual-Energy Unenhanced Head CT at 65–75 KeV Maximizes Image Quality Compared with Conventional Polychromatic CT. *Radiology* **2013**, *266*, 318–325. [CrossRef]
14. Yuan, R.; Shuman, W.P.; Earls, J.P.; Hague, C.J.; Mumtaz, H.A.; Scott-Moncrieff, A.; Ellis, J.D.; Mayo, J.R.; Leipsic, J.A. Reduced Iodine Load at CT Pulmonary Angiography with Dual-Energy Monochromatic Imaging: Comparison with Standard CT Pulmonary Angiography—A Prospective Randomized Trial. *Radiology* **2012**, *262*, 290–297. [CrossRef]
15. Agrawal, M.D.; Pinho, D.F.; Kulkarni, N.M.; Hahn, P.F.; Guimaraes, A.R.; Sahani, D.V. Oncologic Applications of Dual-Energy CT in the Abdomen. *RadioGraphics* **2014**, *34*, 589–612. [CrossRef]
16. De Cecco, C.N.; Darnell, A.; Rengo, M.; Muscogiuri, G.; Bellini, D.; Ayuso, C.; Laghi, A. Dual-Energy CT: Oncologic Applications. *AJR Am. J. Roentgenol.* **2012**, *199* (Suppl. S5), S98–S105. [CrossRef]
17. Silva, A.C.; Morse, B.G.; Hara, A.K.; Paden, R.G.; Hongo, N.; Pavlicek, W. Dual-Energy (Spectral) CT: Applications in Abdominal Imaging. *Radiogr. Rev. Publ. Radiol. Soc. N. Am. Inc.* **2011**, *31*, 1031–1046, Discussion in 1047–1050. [CrossRef]
18. Ferda, J.; Novák, M.; Mírka, H.; Baxa, J.; Ferdová, E.; Bednárová, A.; Flohr, T.; Schmidt, B.; Klotz, E.; Kreuzberg, B. The Assessment of Intracranial Bleeding with Virtual Unenhanced Imaging by Means of Dual-Energy CT Angiography. *Eur. Radiol.* **2009**, *19*, 2518–2522. [CrossRef]
19. Hartman, R.; Kawashima, A.; Takahashi, N.; Silva, A.; Vrtiska, T.; Leng, S.; Fletcher, J.; McCollough, C. Applications of Dual-Energy CT in Urologic Imaging: An Update. *Radiol. Clin.* **2012**, *50*, 191–205. [CrossRef]
20. Nakamura, Y.; Higaki, T.; Honda, Y.; Tatsugami, F.; Tani, C.; Fukumoto, W.; Narita, K.; Kondo, S.; Akagi, M.; Awai, K. Advanced CT Techniques for Assessing Hepatocellular Carcinoma. *Radiol. Med.* **2021**, *126*, 925–935. [CrossRef]
21. Hamid, S.; Nicolaou, S.; Khosa, F.; Andrews, G.; Murray, N.; Abdellatif, W.; Qamar, S.R. Dual-Energy CT: A Paradigm Shift in Acute Traumatic Abdomen. *Can. Assoc. Radiol. J.* **2020**, *71*, 371–387. [CrossRef]
22. Nogel, S.J.; Ren, L.; Yu, L.; Takahashi, N.; Froemming, A.T. Feasibility of Dual-Energy Computed Tomography Imaging of Gadolinium-Based Contrast Agents and Its Application in Computed Tomography Cystography: An Exploratory Study to Assess an Alternative Option When Iodinated Contrast Agents Are Contraindicated. *J. Comput. Assist. Tomogr.* **2021**, *45*, 691–695. [CrossRef]
23. Smith, R.C.; Verga, M.; McCarthy, S.; Rosenfield, A.T. Diagnosis of Acute Flank Pain: Value of Unenhanced Helical CT. *Am. J. Roentgenol.* **1996**, *166*, 97–101. [CrossRef]
24. Ciccarese, F.; Brandi, N.; Corcioni, B.; Golfieri, R.; Gaudiano, C. Complicated Pyelonephritis Associated with Chronic Renal Stone Disease. *Radiol. Med.* **2021**, *126*, 505–516. [CrossRef]
25. Andrabi, Y.; Patino, M.; Das, C.J.; Eisner, B.; Sahani, D.V.; Kambadakone, A. Advances in CT Imaging for Urolithiasis. *Indian J. Urol.* **2015**, *31*, 185. [CrossRef]
26. Nakada, S.Y.; Hoff, D.G.; Attai, S.; Heisey, D.; Blankenbaker, D.; Pozniak, M. Determination of Stone Composition by Noncontrast Spiral Computed Tomography in the Clinical Setting. *Urology* **2000**, *55*, 816–819. [CrossRef]
27. Shahnani, P.S.; Karami, M.; Astane, B.; Janghorbani, M. The Comparative Survey of Hounsfield Units of Stone Composition in Urolithiasis Patients. *J. Res. Med. Sci. Off. J. Isfahan Univ. Med. Sci.* **2014**, *19*, 650–653.
28. Ngo, T.C.; Assimos, D.G. Uric Acid Nephrolithiasis: Recent Progress and Future Directions. *Rev. Urol.* **2007**, *9*, 17–27.
29. Manglaviti, G.; Tresoldi, S.; Guerrer, C.S.; Di Leo, G.; Montanari, E.; Sardanelli, F.; Cornalba, G. In Vivo Evaluation of the Chemical Composition of Urinary Stones Using Dual-Energy CT. *AJR Am. J. Roentgenol.* **2011**, *197*, W76–W83. [CrossRef]
30. Joshi, M.; Langan, D.A.; Sahani, D.S.; Kambadakone, A.; Aluri, S.; Procknow, K.; Wu, X.; Bhotika, R.; Okerlund, D.; Kulkarni, N.; et al. *Effective Atomic Number Accuracy for Kidney Stone Characterization Using Spectral CT*; SPIE: Bellingham, WA, USA, 2010; Available online: https://spie.org/Publications/Proceedings/Paper/10.1117/12.844372?SSO=1 (accessed on 8 June 2023).
31. Flohr, T.G.; McCollough, C.H.; Bruder, H.; Petersilka, M.; Gruber, K.; Süβ, C.; Grasruck, M.; Stierstorfer, K.; Krauss, B.; Raupach, R.; et al. First Performance Evaluation of a Dual-Source CT (DSCT) System. *Eur. Radiol.* **2006**, *16*, 256–268. [CrossRef]

32. Mansouri, M.; Aran, S.; Singh, A.; Kambadakone, A.R.; Sahani, D.V.; Lev, M.H.; Abujudeh, H.H. Dual-Energy Computed Tomography Characterization of Urinary Calculi: Basic Principles, Applications and Concerns. *Curr. Probl. Diagn. Radiol.* **2015**, *44*, 496–500. [CrossRef]
33. Thomas, C.; Patschan, O.; Ketelsen, D.; Tsiflikas, I.; Reimann, A.; Brodoefel, H.; Buchgeister, M.; Nagele, U.; Stenzl, A.; Claussen, C.; et al. Dual-Energy CT for the Characterization of Urinary Calculi: In Vitro and in Vivo Evaluation of a Low-Dose Scanning Protocol. *Eur. Radiol.* **2009**, *19*, 1553–1559. [CrossRef]
34. Jepperson, M.A.; Cernigliaro, J.G.; Ibrahim, E.-S.H.; Morin, R.L.; Haley, W.E.; Thiel, D.D. In Vivo Comparison of Radiation Exposure of Dual-Energy CT Versus Low-Dose CT Versus Standard CT for Imaging Urinary Calculi. *J. Endourol.* **2015**, *29*, 141–146. [CrossRef]
35. Spek, A.; Strittmatter, F.; Graser, A.; Kufer, P.; Stief, C.; Staehler, M. Dual Energy Can Accurately Differentiate Uric Acid-Containing Urinary Calculi from Calcium Stones. *World J. Urol.* **2016**, *34*, 1297–1302. [CrossRef]
36. Lombardo, F.; Bonatti, M.; Zamboni, G.A.; Avesani, G.; Oberhofer, N.; Bonelli, M.; Pycha, A.; Mucelli, R.P.; Bonatti, G. Uric Acid versus Non-Uric Acid Renal Stones: In Vivo Differentiation with Spectral CT. *Clin. Radiol.* **2017**, *72*, 490–496. [CrossRef]
37. Bonatti, M.; Lombardo, F.; Zamboni, G.A.; Pernter, P.; Pycha, A.; Mucelli, R.P.; Bonatti, G. Renal Stones Composition in vivo Determination: Comparison between 100/Sn140 KV Dual-Energy CT and 120 KV Single-Energy CT. *Urolithiasis* **2017**, *45*, 255–261. [CrossRef]
38. Nestler, T.; Nestler, K.; Neisius, A.; Isbarn, H.; Netsch, C.; Waldeck, S.; Schmelz, H.U.; Ruf, C. Diagnostic Accuracy of Third-Generation Dual-Source Dual-Energy CT: A Prospective Trial and Protocol for Clinical Implementation. *World, J. Urol.* **2019**, *37*, 735–741. [CrossRef]
39. Euler, A.; Wullschleger, S.; Sartoretti, T.; Müller, D.; Keller, E.X.; Lavrek, D.; Donati, O. Dual-Energy CT Kidney Stone Characterization—Can Diagnostic Accuracy Be Achieved at Low Radiation Dose? *Eur. Radiol.* **2023**. *Epub ahead of print*. [CrossRef]
40. Kordbacheh, H.; Baliyan, V.; Uppot, R.N.; Eisner, B.H.; Sahani, D.V.; Kambadakone, A.R. Dual-Source Dual-Energy CT in Detection and Characterization of Urinary Stones in Patients with Large Body Habitus: Observations in a Large Cohort. *Am. J. Roentgenol.* **2019**, *212*, 796–801. [CrossRef]
41. Kordbacheh, H.; Baliyan, V.; Singh, P.; Eisner, B.H.; Sahani, D.V.; Kambadakone, A.R. Rapid KVp Switching Dual-Energy CT in the Assessment of Urolithiasis in Patients with Large Body Habitus: Preliminary Observations on Image Quality and Stone Characterization. *Abdom. Radiol.* **2019**, *44*, 1019–1026. [CrossRef]
42. Takahashi, N.; Hartman, R.P.; Vrtiska, T.J.; Kawashima, A.; Primak, A.N.; Dzyubak, O.P.; Mandrekar, J.N.; Fletcher, J.G.; McCollough, C.H. Dual-Energy CT Iodine-Subtraction Virtual Unenhanced Technique to Detect Urinary Stones in an Iodine-Filled Collecting System: A Phantom Study. *AJR Am. J. Roentgenol.* **2008**, *190*, 1169–1173. [CrossRef]
43. Moon, J.W.; Park, B.K.; Kim, C.K.; Park, S.Y. Evaluation of Virtual Unenhanced CT Obtained from Dual-Energy CT Urography for Detecting Urinary Stones. *Br. J. Radiol.* **2012**, *85*, e176–e181. [CrossRef]
44. Wang, J.; Qu, M.; Leng, S.; McCollough, C.H. Differentiation of Uric Acid versus Non-Uric Acid Kidney Stones in the Presence of Iodine Using Dual-Energy CT. In Proceedings of the SPIE Medical Imaging, San Diego, CA, USA, 13–18 February 2010; Volume 7622. [CrossRef]
45. Yeo, Y.J.; Kim, S.H.; Kim, M.J.; Kim, Y.H.; Cho, S.H.; Lee, E.J. Diagnostic Efficiency of Split-Bolus Dual-Energy Computed Tomography for Patients with Suspected Urinary Stones. *J. Comput. Assist. Tomogr.* **2015**, *39*, 25–31. [CrossRef]
46. Magistro, G.; Bregenhorn, P.; Krauß, B.; Nörenberg, D.; D'Anastasi, M.; Graser, A.; Weinhold, P.; Strittmatter, F.; Stief, C.G.; Staehler, M. Optimized Management of Urolithiasis by Coloured Stent-Stone Contrast Using Dual-Energy Computed Tomography (DECT). *BMC Urol.* **2019**, *19*, 29. [CrossRef]
47. Jepperson, M.A.; Cernigliaro, J.G.; Sella, D.; Ibrahim, E.; Thiel, D.D.; Leng, S.; Haley, W.E. Dual-Energy CT for the Evaluation of Urinary Calculi: Image Interpretation, Pitfalls and Stone Mimics. *Clin. Radiol.* **2013**, *68*, e707–e714. [CrossRef]
48. Wisenbaugh, E.S.; Paden, R.G.; Silva, A.C.; Humphreys, M.R. Dual-Energy vs Conventional Computed Tomography in Determining Stone Composition. *Urology* **2014**, *83*, 1243–1247. [CrossRef]
49. Zhang, G.-M.-Y.; Sun, H.; Xue, H.-D.; Xiao, H.; Zhang, X.-B.; Jin, Z.-Y. Prospective Prediction of the Major Component of Urinary Stone Composition with Dual-Source Dual-Energy CT in Vivo. *Clin. Radiol.* **2016**, *71*, 1178–1183. [CrossRef]
50. Shalini, S.; Kasi Arunachalam, V.; Kumar Varatharajaperumal, R.; Mehta, P.; Thambidurai, S.; Cherian, M. The Role of Third-Generation Dual-Source Dual-Energy Computed Tomography in Characterizing the Composition of Renal Stones with Infrared Spectroscopy as the Reference Standard. *Pol. J. Radiol.* **2022**, *87*, 172–176. [CrossRef]
51. Taha, M.; Shawky, M.; Abd Ella, M.D.; Tarek, F. Role of Dual Energy Computed Tomography in Evaluation of Renal Stones. *Med. J. Cairo Univ.* **2021**, *89*, 1349–1357. [CrossRef]
52. Galluzzo, A.; Danti, G.; Bicci, E.; Mastrorosato, M.; Bertelli, E.; Miele, V. The Role of Dual-Energy CT in the Study of Urinary Tract Tumors: Review of Recent Literature. *Semin. Ultrasound CT MRI* **2023**, *44*, 136–144. [CrossRef]
53. Graser, A.; Becker, C.R.; Staehler, M.; Clevert, D.A.; Macari, M.; Arndt, N.; Nikolaou, K.; Sommer, W.; Stief, C.; Reiser, M.F.; et al. Single-Phase Dual-Energy CT Allows for Characterization of Renal Masses as Benign or Malignant. *Investig. Radiol.* **2010**, *45*, 399–405. [CrossRef]
54. Pourvaziri, A.; Mojtahed, A.; Hahn, P.F.; Gee, M.S.; Kambadakone, A.; Sahani, D.V. Renal Lesion Characterization: Clinical Utility of Single-Phase Dual-Energy CT Compared to MRI and Dual-Phase Single-Energy CT. *Eur. Radiol.* **2023**, *33*, 1318–1328. [CrossRef] [PubMed]

55. McGrath, T.A.; Ahmad, F.; Sathiadoss, P.; Haroon, M.; McInnes, M.D.; Bossuyt, P.M.; Schieda, N. Direct Comparison of Diagnostic Accuracy of Fast Kilovoltage Switching Dual-Energy Computed Tomography and Magnetic Resonance Imaging for Detection of Enhancement in Renal Masses. *J. Comput. Assist. Tomogr.* **2022**, *46*, 862–870. [CrossRef] [PubMed]
56. Marcon, J.; Graser, A.; Horst, D.; Casuscelli, J.; Spek, A.; Stief, C.G.; Reiser, M.F.; Rübenthaler, J.; Buchner, A.; Staehler, M. Papillary vs Clear Cell Renal Cell Carcinoma. Differentiation and Grading by Iodine Concentration Using DECT-Correlation with Microvascular Density. *Eur. Radiol.* **2020**, *30*, 1–10. [CrossRef] [PubMed]
57. Jonisch, A.I.; Rubinowitz, A.N.; Mutalik, P.G.; Israel, G.M. Can High-Attenuation Renal Cysts Be Differentiated from Renal Cell Carcinoma at Unenhanced CT? *Radiology* **2007**, *243*, 445–450. [CrossRef] [PubMed]
58. Graser, A.; Johnson, T.R.C.; Hecht, E.M.; Becker, C.R.; Leidecker, C.; Staehler, M.; Stief, C.G.; Hildebrandt, H.; Godoy, M.C.B.; Finn, M.E.; et al. Dual-Energy CT in Patients Suspected of Having Renal Masses: Can Virtual Nonenhanced Images Replace True Nonenhanced Images? *Radiology* **2009**, *252*, 433–440. [CrossRef]
59. Thiravit, S.; Brunnquell, C.; Cai, L.M.; Flemon, M.; Mileto, A. Use of Dual-Energy CT for Renal Mass Assessment. *Eur. Radiol.* **2021**, *31*, 3721–3733. [CrossRef]
60. Arndt, N.; Staehler, M.; Siegert, S.; Reiser, M.F.; Graser, A. Dual Energy CT in Patients with Polycystic Kidney Disease. *Eur. Radiol.* **2012**, *22*, 2125–2129. [CrossRef]
61. Cha, D.; Kim, C.K.; Park, J.J.; Park, B.K. Evaluation of Hyperdense Renal Lesions Incidentally Detected on Single-Phase Post-Contrast CT Using Dual-Energy CT. *Br. J. Radiol.* **2016**, *89*, 20150860. [CrossRef]
62. Ascenti, G.; Mazziotti, S.; Mileto, A.; Racchiusa, S.; Donato, R.; Settineri, N.; Gaeta, M. Dual-Source Dual-Energy CT Evaluation of Complex Cystic Renal Masses. *AJR Am. J. Roentgenol.* **2012**, *199*, 1026–1034. [CrossRef]
63. Moleesaide, A.; Maneegarn, A.; Kaewlai, R.; Thiravit, S. Virtual Monochromatic Spectral Attenuation Curve Analysis for Evaluation of Incidentally Detected Small Renal Lesions Using Rapid Kilovoltage-Switching Dual-Energy Computed Tomography. *Abdom. Radiol.* **2022**, *47*, 3817–3827. [CrossRef]
64. Wei, J.; Zhao, J.; Zhang, X.; Wang, D.; Zhang, W.; Wang, Z.; Zhou, J. Analysis of Dual Energy Spectral CT and Pathological Grading of Clear Cell Renal Cell Carcinoma (CcRCC). *PLoS ONE* **2018**, *13*, e0195699. [CrossRef]
65. Greco, F.; Mallio, C.A. Relationship between Visceral Adipose Tissue and Genetic Mutations (VHL and KDM5C) in Clear Cell Renal Cell Carcinoma. *Radiol. Med.* **2021**, *126*, 645–651. [CrossRef]
66. Walker, D.; Udare, A.; Chatelain, R.; McInnes, M.; Flood, T.; Schieda, N. Utility of Material-Specific Fat Images Derived from Rapid-KVp-Switch Dual-Energy Renal Mass CT for Diagnosis of Renal Angiomyolipoma. *Acta Radiol.* **2021**, *62*, 1263–1272. [CrossRef]
67. Çamlıdağ, İ.; Nural, M.S.; Danacı, M.; Özden, E. Usefulness of Rapid KV-Switching Dual Energy CT in Renal Tumor Characterization. *Abdom. Radiol.* **2019**, *44*, 1841–1849. [CrossRef]
68. Alanee, S.; Dynda, D.I.; Hemmer, P.; Schwartz, B. Low Enhancing Papillary Renal Cell Carcinoma Diagnosed by Using Dual Energy Computerized Tomography: A Case Report and Review of Literature. *BMC Urol.* **2014**, *14*, 102. [CrossRef] [PubMed]
69. Uroweb—European Association of Urology. Non-Muscle-Invasive Bladder Cancer—Introduction—Uroweb. Available online: https://uroweb.org/guidelines/non-muscle-invasive-bladder-cancer (accessed on 14 May 2023).
70. Takeuchi, M.; McDonald, J.S.; Takahashi, N.; Frank, I.; Thompson, R.H.; King, B.F.; Kawashima, A. Cancer Prevalence and Risk Stratification in Adults Presenting with Hematuria: A Population-Based Cohort Study. *Mayo Clin. Proc. Innov. Qual. Outcomes* **2021**, *5*, 308–319. [CrossRef] [PubMed]
71. De Cecco, C.N.; Buffa, V.; Fedeli, S.; Vallone, A.; Ruopoli, R.; Luzietti, M.; Miele, V.; Rengo, M.; Maurizi Enrici, M.; Fina, P.; et al. Preliminary Experience with Abdominal Dual-Energy CT (DECT): True versus Virtual Nonenhanced Images of the Liver. *Radiol. Med.* **2010**, *115*, 1258–1266. [CrossRef] [PubMed]
72. Buffa, V.; Solazzo, A.; D'Auria, V.; Del Prete, A.; Vallone, A.; Luzietti, M.; Madau, M.; Grassi, R.; Miele, V. Dual-Source Dual-Energy CT: Dose Reduction after Endovascular Abdominal Aortic Aneurysm Repair. *Radiol. Med.* **2014**, *119*, 934–941. [CrossRef]
73. Helenius, M.; Dahlman, P.; Magnusson, M.; Lönnemark, M.; Magnusson, A. Contrast Enhancement in Bladder Tumors Examined with CT Urography Using Traditional Scan Phases. *Acta Radiol.* **2014**, *55*, 1129–1136. [CrossRef]
74. Raman, S.P.; Fishman, E.K. Bladder Malignancies on CT: The Underrated Role of CT in Diagnosis. *Am. J. Roentgenol.* **2014**, *203*, 347–354. [CrossRef]
75. Sahni, V.A.; Shinagare, A.B.; Silverman, S.G. Virtual Unenhanced CT Images Acquired from Dual-Energy CT Urography: Accuracy of Attenuation Values and Variation with Contrast Material Phase. *Clin. Radiol.* **2013**, *68*, 264–271. [CrossRef] [PubMed]
76. Chow, L.C.; Kwan, S.W.; Olcott, E.W.; Sommer, G. Split-Bolus MDCT Urography with Synchronous Nephrographic and Excretory Phase Enhancement. *AJR Am. J. Roentgenol.* **2007**, *189*, 314–322. [CrossRef] [PubMed]
77. Chen, C.-Y.; Tsai, T.-H.; Jaw, T.-S.; Lai, M.-L.; Chao, M.-F.; Liu, G.-C.; Hsu, J.-S. Diagnostic Performance of Split-Bolus Portal Venous Phase Dual-Energy CT Urography in Patients with Hematuria. *AJR Am. J. Roentgenol.* **2016**, *206*, 1013–1022. [CrossRef] [PubMed]
78. Johnson, T.R.C. Dual-Energy CT: General Principles. *AJR Am. J. Roentgenol.* **2012**, *199* (Suppl. S5), S3–S8. [CrossRef]
79. Zopfs, D.; Laukamp, K.R.; dos Santos, D.P.; Sokolowski, M.; Hokamp, N.G.; Maintz, D.; Borggrefe, J.; Persigehl, T.; Lennartz, S. Low-KeV Virtual Monoenergetic Imaging Reconstructions of Excretory Phase Spectral Dual-Energy CT in Patients with Urothelial Carcinoma: A Feasibility Study. *Eur. J. Radiol.* **2019**, *116*, 135–143. [CrossRef]

80. Uroweb—European Association of Urology. EAU Guidelines on Upper Urinary Tract Urothelial Cell Carcinoma—Introduction—Uroweb. Available online: https://uroweb.org/guidelines/upper-urinary-tract-urothelial-cell-carcinoma (accessed on 14 May 2023).
81. Lee, K.Y.G.; Cheng, H.M.J.; Chu, C.Y.; Tam, C.W.A.; Kan, W.K. Metal Artifact Reduction by Monoenergetic Extrapolation of Dual-Energy CT in Patients with Metallic Implants. *J. Orthop. Surg.* **2019**, *27*, 2309499019851176. [CrossRef]
82. Bamberg, F.; Dierks, A.; Nikolaou, K.; Reiser, M.F.; Becker, C.R.; Johnson, T.R.C. Metal Artifact Reduction by Dual Energy Computed Tomography Using Monoenergetic Extrapolation. *Eur. Radiol.* **2011**, *21*, 1424–1429. [CrossRef]
83. Lewis, M.; Reid, K.; Toms, A.P. Reducing the Effects of Metal Artefact Using High KeV Monoenergetic Reconstruction of Dual Energy CT (DECT) in Hip Replacements. *Skelet. Radiol.* **2013**, *42*, 275–282. [CrossRef]
84. Higashigaito, K.; Angst, F.; Runge, V.M.; Alkadhi, H.; Donati, O.F. Metal Artifact Reduction in Pelvic Computed Tomography with Hip Prostheses: Comparison of Virtual Monoenergetic Extrapolations from Dual-Energy Computed Tomography and an Iterative Metal Artifact Reduction Algorithm in a Phantom Study. *Investig. Radiol.* **2015**, *50*, 828–834. [CrossRef]
85. Bicci, E.; Mastrorosato, M.; Danti, G.; Lattavo, L.; Bertelli, E.; Cozzi, D.; Pradella, S.; Agostini, S.; Miele, V. Dual-Energy CT Applications in Urinary Tract Cancers: An Update. *Tumori* **2023**, *109*, 148–156. [CrossRef] [PubMed]
86. Nakagawa, M.; Naiki, T.; Naiki-Ito, A.; Ozawa, Y.; Shimohira, M.; Ohnishi, M.; Shibamoto, Y. Usefulness of Advanced Monoenergetic Reconstruction Technique in Dual-Energy Computed Tomography for Detecting Bladder Cancer. *Jpn. J. Radiol.* **2022**, *40*, 177–183. [CrossRef] [PubMed]
87. Hansen, C.; Becker, C.D.; Montet, X.; Botsikas, D. Diagnosis of Urothelial Tumors with a Dedicated Dual-Source Dual-Energy MDCT Protocol: Preliminary Results. *Am. J. Roentgenol.* **2014**, *202*, W357–W364. [CrossRef] [PubMed]
88. Wrixon, A.D. New ICRP Recommendations. *J. Radiol. Prot.* **2008**, *28*, 161–168. [CrossRef]
89. Agostini, A.; Borgheresi, A.; Carotti, M.; Ottaviani, L.; Badaloni, M.; Floridi, C.; Giovagnoni, A. Third-Generation Iterative Reconstruction on a Dual-Source, High-Pitch, Low-Dose Chest CT Protocol with Tin Filter for Spectral Shaping at 100 KV: A Study on a Small Series of COVID-19 Patients. *Radiol. Med.* **2021**, *126*, 388–398. [CrossRef]
90. Apfaltrer, G.; Dutschke, A.; Baltzer, P.A.T.; Schestak, C.; Özsoy, M.; Seitz, C.; Veser, J.; Petter, E.; Helbich, T.H.; Ringl, H.; et al. Substantial Radiation Dose Reduction with Consistent Image Quality Using a Novel Low-Dose Stone Composition Protocol. *World J. Urol.* **2020**, *38*, 2971–2979. [CrossRef]
91. Dewes, P.; Frellesen, C.; Scholtz, J.-E.; Fischer, S.; Vogl, T.J.; Bauer, R.W.; Schulz, B. Low-Dose Abdominal Computed Tomography for Detection of Urinary Stone Disease—Impact of Additional Spectral Shaping of the X-ray Beam on Image Quality and Dose Parameters. *Eur. J. Radiol.* **2016**, *85*, 1058–1062. [CrossRef]
92. Marin, D.; Boll, D.T.; Mileto, A.; Nelson, R.C. State of the Art: Dual-Energy CT of the Abdomen. *Radiology* **2014**, *271*, 327–342. [CrossRef]
93. Mileto, A.; Marin, D.; Nelson, R.C.; Ascenti, G.; Boll, D.T. Dual Energy MDCT Assessment of Renal Lesions: An Overview. *Eur. Radiol.* **2014**, *24*, 353–362. [CrossRef]
94. Parakh, A.; An, C.; Lennartz, S.; Rajiah, P.; Yeh, B.M.; Simeone, F.J.; Sahani, D.V.; Kambadakone, A.R. Recognizing and Minimizing Artifacts at Dual-Energy CT. *Radiogr. Rev. Publ. Radiol. Soc. N. Am. Inc.* **2021**, *41*, 509–523. [CrossRef]
95. Lambert, J.W.; FitzGerald, P.F.; Edic, P.M.; Sun, Y.; Bonitatibus, P.J.; Colborn, R.E.; Yeh, B.M. The Effect of Patient Diameter on the Dual-Energy Ratio of Selected Contrast-Producing Elements. *J. Comput. Assist. Tomogr.* **2017**, *41*, 505–510. [CrossRef] [PubMed]
96. Borges, A.P.; Antunes, C.; Curvo-Semedo, L. Pros and Cons of Dual-Energy CT Systems: "One Does Not Fit All". *Tomography* **2023**, *9*, 195–216. [CrossRef] [PubMed]
97. Dual-Energy CT: Is It What the Doctor Ordered for the Cost-Conscious Community Hospital? Available online: https://radiologybusiness.com/sponsored/1081/hitachi-healthcare-americas/topics/healthcare-management/healthcare-economics/dual (accessed on 14 May 2023).